CAMBRIDGE
UNIVERSITY PRESS

RESEARCH ARTICLE

A new comprehensive performance optimization approach for Earth-contact mechanism based on terrain-adaptability task

Hongyan Tang[1], James M. Zhang[2] and Dan Zhang[1,3,*]

[1]Institute of AI and Robotics, Academy for Engineering and Technology, Fudan University, Shanghai 200433, Republic of China, [2]McMaster University, Hamilton, ON L8S 4L8, Canada, and [3]Department of Mechanical Engineering, Lassonde School of Engineering, York University, Toronto, ON M3J 1P3, Canada
*Corresponding author. E-mail: dzhang99@yorku.ca

Abstract

Earth-contact mechanism (ECM), a type of mechanism to keep the system in contact with the earth and to move with the terrain changes. This paper uses the virtual equivalent parallel mechanism (VEPM) to convert the terrain data into the kinematical variables of the moving platform in the VEPM, and further analyzes the performance of the VEPM at each terrain point. Then, the comprehensive performance of the VEPM is chosen as the optimization goal, and a task-oriented dimensional optimization approach combined with the particle swarm algorithm and the neural network algorithm is proposed. This paper conducted a comparative experiment to verify the superiority of the new approach in optimizing the ECM's comprehensive performance, whose performance analysis also can be applied into the layout design of the ECM. This paper proposed an analysis method to construct the ECM's performance map based on the digital terrain map, which helps the control system and operator to make the optimal control decision.

1. Introduction

In the fields of automobiles, aviation, mobile robots, etc., there is a type of mechanism whose function is to keep the system in contact with the earth and to move following the terrain changes. This paper names this type of mechanism as the earth-contact mechanism (ECM). For example, the vehicle's suspension [1] keeps four wheels in contact with the ground and adjusts the stroke to mitigate the impact of the terrain changes. Therefore, the suspension can be regarded as an ECM. Similarly, the landing gear of aircrafts [2], the lander of planetary probes [3], the suspension of multihulls [4], the legs of bionic robots [5], and quadruped robots [6], etc. can all be regarded as the ECM.

For different application fields, the design of the ECM has different performance requirements. Therefore, the task-oriented performance optimization is a core issue in the engineering design of the ECM. Present researches proposed various specific optimization methods for different performance requirements.

For the optimization of the legged robot, Russoa et al. [7] optimized a 3-UPR mechanism by taking the volume of the workspace [8], the operating flexibility [9], the static efficiency [10], and the stiffness [11] as the comprehensive optimization goal. Zhang et al. [12] optimized the dimension of a planar multi-link mechanism by taking the torque, speed, and endurance performances as the optimization goal.

For alien detectors, Gao et al. [13] proposed a four-leg reconfigurable mechanism and optimized the workspace volume [14], the Walking step index [13], the global transfer index [15, 16], the global speed index [17], the global load index [18], and the global stiffness index [19] of the mechanism in

the landing posture and moving configuration. Lin et al. [20] designed a serial of legged mobile landers with a passive limb and singularity property.

For the suspension system, Niessing et al. [21] take the design space, the kinematics model, and the elastokinematic as the boundary conditions and optimize the suspension characteristics and weight factor of the vehicle. Issa et al. [22] applied the HHO optimization algorithm into optimizing the acceleration peak, the dynamic tire load, and the displacement peak performance in the suspension system. Edgar [23] proposed a kinematic model comprises 12 degrees of freedom (DOF) for active drive four-wheel robot structures and designed a general kinematic control law.

By analyzing and comparing the above researches, two common features of these optimization method can be summarized: first, ECMs are analyzed and optimized for a single chain mechanism, not the whole system. Second, these performance analyses are established on the general workspace, not the specific task space. In this way, the optimal theoretical design is hard to achieve the best performance in the practical application. Thus, it is necessary to take the overall system of the ECM as the analysis object and then optimize the dimensions of the ECM based on the specific task spaces.

The task-oriented performance optimization has been studied by many scholars based on specific application scenarios. Yu [24] optimized geometrical parameters of a parallel manipulator according to a specific spray-painting task. Wu et al. [25] proposed a multiobjective optimal design for a novel 6-DOFs hybrid spray-painting robot based on the compactness, motion/force transmissibility, and energy consumption analysis. Wan et al. [26] optimized the mobile and grabbing performance of a walkable fixture mechanism by adding constraints on the workspace. According to the characteristics of the grasping task, Wu et al. [27] optimized the performance of the parallel Schönflies-motion robot based on the given rectangular workspace. Based on requirements of the surface machining, Kim et al. [28] designed a six DOFs redundant driving parallel mechanism with a circular orbit. Gao et al. [29] designed a 6 DOFs parallel motion simulator based on the given task workspace. The above-mentioned studies describe the functional task by limiting the workspace. However, the workspace with the restriction is still evenly distributed, but the task space of the ECM is usually unevenly distributed.

Since the main object of the ECM is the terrain, the specific task space of the ECM can be described by the terrain data. In the literature [30, 31], the terrain data are converted into characteristic values such as slope, roughness, and step height to analyze the adaptability of the mechanism. By solving the intersection of the fitting terrain surface and the workspace of the mechanism [32, 33], the posture set matching the terrain can be obtained. Based on the feasible posture set, the comprehensive performance of the ECM can be analyzed [34], and it can also be used for the optimal decision making of the control system [35, 36]. The above researches have laid the foundation of the parametric expression of the ECM's task space. This paper will further study the expression method of the ECM's functional task.

On the other hand, to model the entire system of the ECM, the ECM and the terrain can be regarded as a whole analysis object. The kinematic chain of the ECM connects the base and the terrain, respectively, which is similar to the parallel mechanism. Therefore, the mechanism-terrain can be analyzed as a parallel mechanism.

The similar concept first appears in the literature [37] first. Likar et al. [37] taken a dual-arm manipulation and the target object as a joined kinematic chain. Ozgur et al. [38] taken the dexterous hand and the grasping object as a parallel mechanism and proposes the concept of the equivalent parallel mechanism. Hu et al. [39] introduced this idea to a legged robot and judged the DOF of the robot by analyzing the foot-contact type. Reference [33] studied the modeling and performance analysis of the virtual equivalent parallel mechanism based on the adaptive landing gear mechanism. These studies provide an ideal solution for constructing the mechanism-terrain system model.

To apply the mechanism-terrain modeling method to the task-oriented dimensional synthesis of the ECM, this paper studied the parametric expression of the ECM's functional task and analyze the performance of the mechanism-terrain system. ECM's functional task and its parametric conversion method are introduced and analyzed in Section 2; the VEPM model of the ECM, the kinematics and performance analysis of the VEPM are introduced in Section 3; the effectiveness of the new approach is verified in Section 4; finally, conclusions are summarized in Section 5.

2. Digital quantification of the functional task

The core issue of the task-oriented performance optimization is the digital quantification analysis of the functional task. There are two main problems within the core issue: first, how to transform the description of the functional task into a parametric expression. Second, how to convert the parametric expression into the performance indexes of the mechanism. In this section, we will focus on the first key problem and deduce the parametric expression of the ECM functional task. The second key question will be analyzed and discussed in Section 3.

2.1. Function analysis

At first, this paper declares that the ECM is just a unified name of the mechanism with the two characteristics mentioned in Section 1, not a new mechanism. The main function of the ECM is to respond to terrain changes, and this function is named terrain adaptability in this paper. Compared with terrain adaptability (visualizes the adaptations of organisms with topographic models) proposed by Wright [40], terrain adaptability in this paper is mainly used to evaluate the adaptability of the mechanism to the terrain surface.

The terrain adaptability can be divided into three aspects. The first, adaptability, is the ability of ECM to maintain a stable posture at that terrain point. The more adaptable the ECM is, the wider the terrain range the ECM can match, and the larger the volume of the ECM's workspace is required. Second, the kinematic ability is the kinematical performance of the ECM when the mechanism follows the terrain change. When the mechanism has the stronger kinematic ability, it matches the terrain changes more quickly and efficiently. Third, stability is the ability of the ECM to resist overturning at the terrain point. The stronger the stability of the ECM, the greater the external disturbance it can resist in that terrain point, and the higher the reliability and safety of the system.

In summary, the general functional requirements of the ECM are strong adaptability, fast and efficient kinematic ability, and high stability.

2.2. Task analysis

According to different application scenarios, the functional tasks of the ECM are different. For the vehicle's suspension and shock absorption system, the ECM is required to have a light impact on the vehicle body when the vehicle is in driving. For the adaptive landing gear of a vertical taking-off and landing aircraft, the ECM needs to adapt the terrain area as large as possible. For the construction machinery, the ECM needs a strong stability during the operation. Obviously, different functional tasks have different requirements for the ECM's performance. However, these performance requirements correspond exactly to the three performance indexes in the terrain adaptability. Therefore, this paper uses these three performance indexes to evaluate the functional tasks of the ECM.

Before evaluating the performance of the ECM, the ECM's task object needs to be clarified first. Considering that the terrain is the main contact object of the ECM, this paper takes the terrain as the description object of the functional task. The digital elevation map (DEM) is widely used to descript the terrain surface. The DEM model is a digital simulation of ground terrain through limited terrain elevation data. The DEM is expressed in the form of a set of ordered numerical matrix and is widely used in the hydrographic surveying and mapping, the meteorological geology, the engineering construction, etc. [41]. Therefore, the DEM model is adopted as the digital expression of the terrain in this paper.

Taking the DEM model as the functional task object, the ECM's task scope could be further determined. The classical performance analysis of a mechanism takes the workspace of the mechanism as the task scope, and the comprehensive performance index of the mechanism is the integral result of the local performance index in the whole workspace. However, all the ECM's working points on the specific terrain surface are nonuniformly distributed in the ECM's classical workspace (the workspace solved by classical method [8, 14]). So, the classical performance analysis method is unsuitable for specific functional tasks. Therefore, this paper analyzes the ECM's performance based on the parametric terrain surface and uses its result as the quantitative index of the functional task.

2.3. Parametric conversion of the functional task

After the functional task analysis of the ECM, the parametric conversion of the functional task is transformed into the mapping relationship from the DEM model to the comprehensive performance index of the ECM. This section will derive the mapping relationship in detail.

The first step is to construct the terrain surface. The DEM model is obtained from aircrafts or satellites by scanning the ground. The DEM model is expressed in a matrix. The rows and columns of the matrix correspond to the latitude and longitude coordinates of the terrain point, while the value in the matrix is the height value. However, the matrix expression of the DEM has two limitations.

Limitation 1: The matrix is a set of finite values, and the height data are discretized. To analyze and solve the contact points of the ECM at the terrain point, it is necessary to make the discrete height data continuous. In this paper, the spline surface fitting method is used to realize the continuity of discrete points. Fifteen terrain points adjacent to the target terrain point are used to construct the fitting surface. The parameterized expression of the fitting surface $S(u,v)$ at the terrain point is shown in Eq. (1).

$$
\begin{aligned}
S(u, v) &= \sum_{i=0}^{3} \sum_{j=0}^{3} N_{i,p}(u)\, N_{j,p}(v)\, P_{i,j} \\
N_{i,0}(u) &= \begin{cases} 1\,(\text{if } u_i \leq u < u_{i+1}) \\ 0\,(\text{otherwise}) \end{cases} \\
N_{i,p}(u) &= \frac{u - u_i}{u_{i+p} - u_i} N_{i,p-1}(u) + \frac{u_{i+p+1} - u}{u_{i+p+1} - u_{i+1}} N_{i+1,p-1}(u)
\end{aligned}
\tag{1}
$$

where $P_{i,j}$ is the height at the ith and jth terrain point, N is the spline coefficient, and $p = 3$ is the order of the base function.

Limitation 2: The distance between the two adjacent terrain points is too far, and its order of magnitude (OFM) is decameter level. The OFM of the distance is higher than that of the mechanism dimension. It means that the performance solved from the DEM model may not completely equal to the actual situation. However, in the statistics, the calculation result can present the average value of the performance index in the adjacent areas. Therefore, this paper regards the performance calculated at the terrain point as the actual performance.

The second step is to solve the kinematic model of the ECM at the terrain point. The classical mechanism kinematics is the mapping function between the input variables (or driving variables) and the output variables of the mechanism. The terrain data of the ECM at the terrain point are neither the input variable nor the output variable of the mechanism. So, it is necessary to convert the terrain data into the kinematical variables of the mechanism first. According to the literature [33, 34], the terrain data can be converted into the kinematical parameters of the moving platform through the VEPM model. The detailed conversion will be introduced in Section 3. Then, according to the kinematical model of the VEPM, the kinematical parameters of the ECM can be solved.

The third step is to solve the comprehensive performance index of the ECM. Referring to the classical comprehensive performance solution, the comprehensive performance index of the ECM can also be decomposed into two processes. The first process is to solve the local performance index of the ECM at the terrain point and to construct the local performance map based on the terrain map. The second process is the integral operation of the local performance map to solve the comprehensive performance index S_g of the ECM, as shown in Eq. (2).

$$
S_g = \int_T S_l \Big/ V_T
\tag{2}
$$

where T is the target terrain map, V_T is the workspace volume, S_l is the local performance index, and S_T is the workspace volume with the target terrain map.

The conversion process of the digital quantification of the functional task is shown in Fig. 1. First, according to the DEM model, the parametric surface at the terrain point is solved. Then, combining the VEPM model and the kinematical model of the original mechanism, the kinematical parameters of
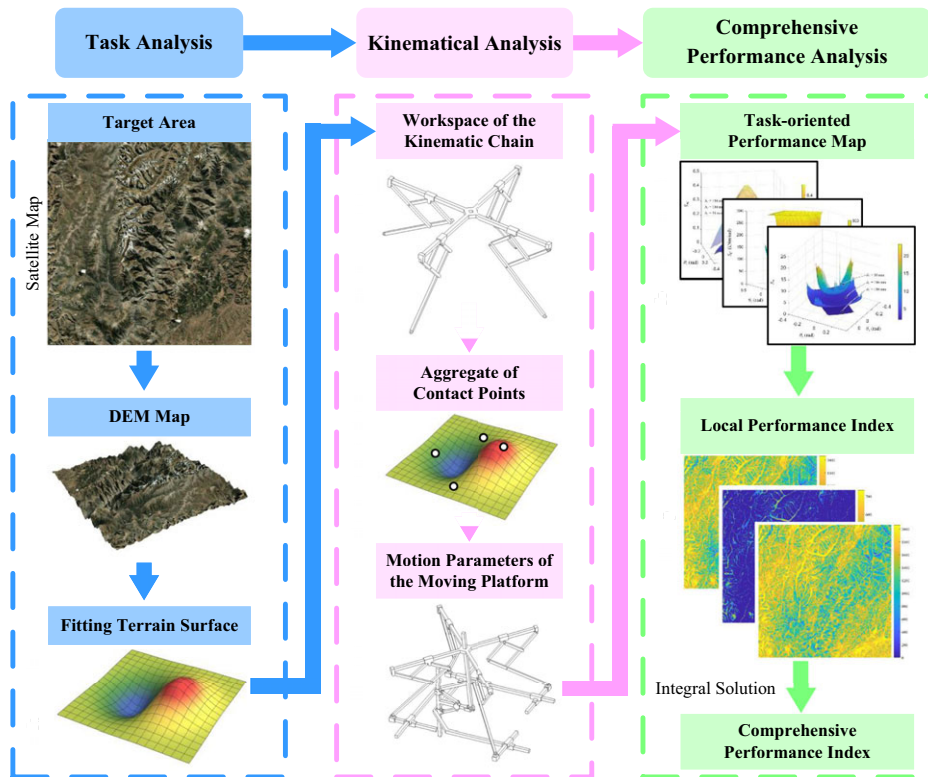
Figure 1. *The flowchart of the conversion process.*

the ECM at the terrain points are solved. Finally, the comprehensive performance of the ECM with the functional task can be obtained by solving the local performance map of the ECM.

3. Task-oriented comprehensive performance optimization Approach

Another core issue to achieve task-oriented performance optimization of the ECM is how to translate the terrain data to the mechanism performance indexes. In the literature [33, 34], the virtual equivalent parallel mechanism (VEPM) method is proposed and applied to the performance analysis of the terrain-adaptive landing gear. This paper will also quote the VEPM model to derive the performance analysis and dimensional optimization step by step. This section will first introduce the VEPM model of the ECM, then analyze the performance indexes of the VEPM model, and finally introduce the performance optimization approach of the ECM.

3.1. Virtual equivalent parallel mechanism model

According to the research on the VEPM in the literatures [33, 34], the construction of VEPM model mainly includes three processes of the decomposition, construction, and combination. The main elements of the VEPM model include the original mechanism, the virtual restraint chain (VRC), the virtual kinematical chain (VKC), and the virtual moving platform (VMP). By comparing the conclusions of the two references [33, 34], it can be found that the VMP's structure varies according to the number of chains in the original mechanism, while the VRC's and VKC's structure are the same. In the existing industrial applications, three-leg (aircraft landing gear, etc.) and four-leg (car suspension, quadruped robot, etc.)
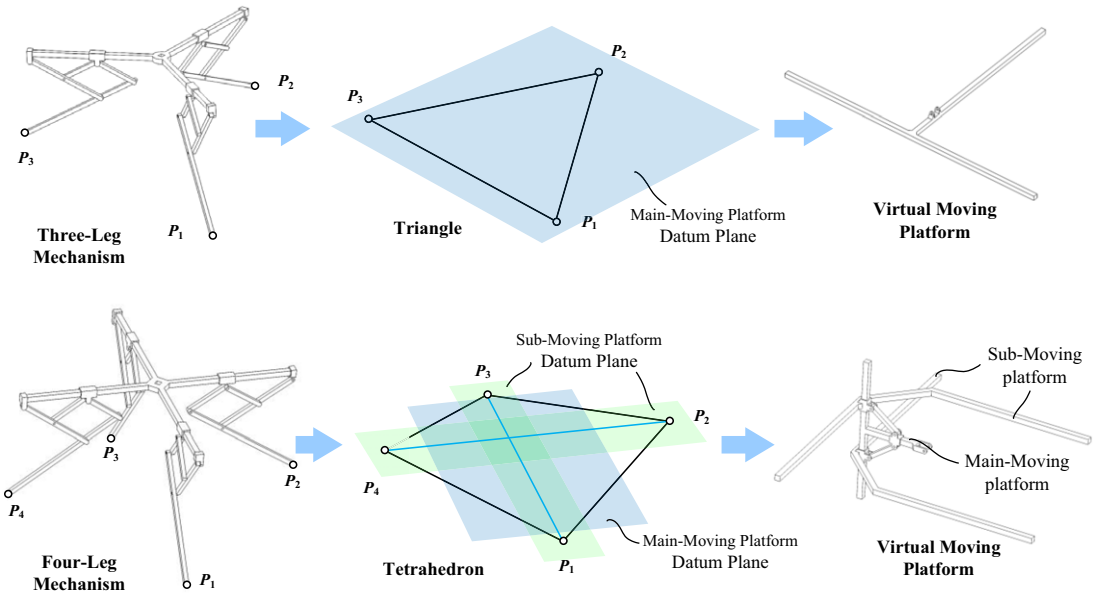
Figure 2. *The construction of VPMs.*

layouts are the most widely used layout in the ECMs. Therefore, this paper will focus on the analysis of the three-leg and four-leg ECMs.

3.1.1. Construction of the VEPM

The construction of virtual components in the VEPM model mainly includes the construction of VMP, VRC, and VKC.

The virtual moving platform (VMP) is constructed according to the relative potion of the touch points. The number of the touch points depends on the number of chains in the original mechanism. The three-leg ECM has three touch points, and a plane passing through those three touch points can be used as the datum plane of the VMP. The four-leg ECM has four contact points, and a spatial tetrahedron can be used as the VMP. The parallelogram plane formed by the midpoints of the adjacent contact points is used as the datum plane of the main-VMP. Two sub-VMPs are constructed based on the diagonals of the spatial tetrahedron. The construction process of the VPMs is shown in Fig. 2.

The VRC is set up to restrain the motion of the VMP. The datum plane of the VMP (or main-VMP) has two rotation DOFs and one translational DOF referring to the base coordinate system. Therefore, a universal (U) pair and a prismatic (P) pair are used as the VRC of VEPM, as shown in Fig. 3.

The VKC is constructed to connect the original kinematic chain of the ECM and the VMP. Then, the VKC must have a restricted force perpendicular to the datum plane of the VMP. In this paper, a spherical (S) pair and 2 P pairs are used as the VKC of the VEPM, as shown in Fig. 3.

Finally, the VEPM is obtained by combining the constructed virtual components with the original mechanism. The VRC connects the center of the ECM base and the center of the VMP. The VKC is connected with kinematic chain of the ECM and the VMP at the contact point.

3.1.2. Kinematics of the VEPM

The kinematical model of the VEPM is the relationship between the driving variables of the ECM and the kinematic variables of the VMP. The kinematical model can be derived through the position of the touch points.
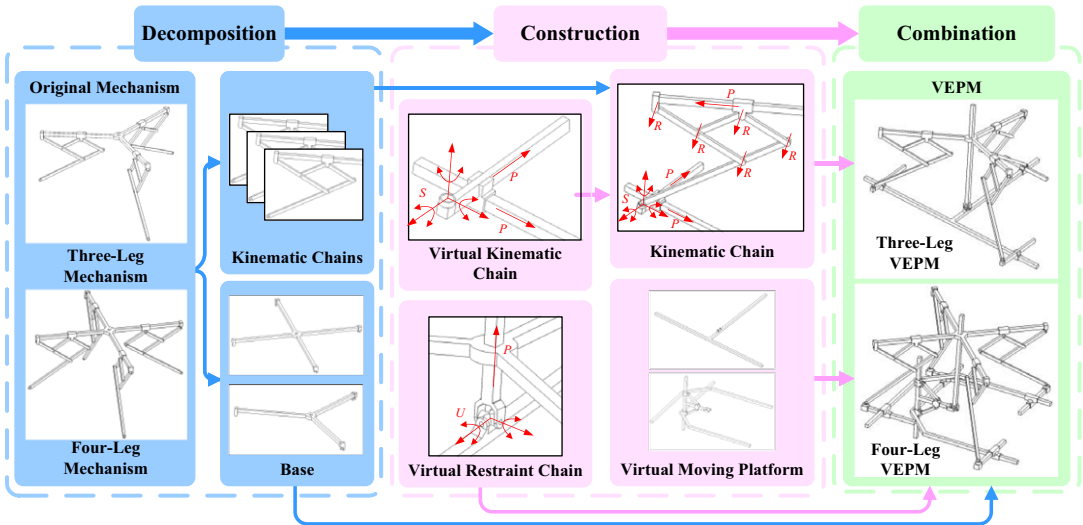
Figure 3. *The construction of VEPMs.*

First, according to the kinematical model of the original mechanism, the relationship between the driving variables and the position of the touch points is obtained, as shown in Eq. (3).

$$P_i = F_f(q_i) \tag{3}$$

where P_i and q_i are the touch point coordinates and the driving variable of the ith kinematic chain, and F_f is the forward kinematical model.

Then, based on the position of the touch points, the parametric equation of the datum plane of the VMP can be solved. Equation (4) shows the equations for the 3-legged mechanism, while Eq. (5) for the 4-legged mechanism.

$$n_z \cdot P + d = 0$$
$$n_z = R_{XY} \cdot \left\{ \begin{matrix} 0 & 0 & 1 \end{matrix} \right\}^T = \left\{ \begin{matrix} n_{z,x} & n_{z,y} & n_{z,z} \end{matrix} \right\}^T = \frac{(P_2 - P_1) \times (P_3 - P_1)}{norm((P_2 - P_1) \times (P_3 - P_1))} \tag{4}$$

where n_z is the unit normal vector of the datum plane, and d is a constant $d = h_c \cdot n_z$.

$$n_z \cdot P + d + \frac{1}{2}d_m = 0$$
$$n_z \cdot P + d - \frac{1}{2}d_m = 0$$
$$n_z = R_{XY} \cdot \left\{ \begin{matrix} 0 & 0 & 1 \end{matrix} \right\}^T = \left\{ \begin{matrix} n_{z,x} & n_{z,y} & n_{z,z} \end{matrix} \right\}^T = \frac{(P_3 - P_1) \times (P_4 - P_2)}{norm((P_3 - P_1) \times (P_4 - P_2))} \tag{5}$$

where d_m is the distance between the two sub-MPs.

Combining the Euler angle and the rotation matrix, the rotation variables θ_x and θ_y of the VMP can be calculated, as shown in Eq. (5).

$$\theta_x = \arcsin(-n_{z,y})$$
$$\theta_y = \arctan\left(n_{z,x} \Big/ n_{z,z}\right) \tag{6}$$
$$h_c = d \Big/ n_{z,z}$$

The above calculation process is the forward kinematical model of the VEPM. Conversely, the inverse kinematics of the VEPM can be solved.

The Jacobian matrix of the VEPM is the mapping relationship between the velocities of the driving joint in the ECM and the motion speed of the VMP. At touch points, the velocities of the ECM are equal to that of the VMP, and the following relationship can be obtained in Eq. (6)

$$J_X \dot{X} = V_T = J_q \dot{q}$$

$$
J_X =
\begin{cases}
\begin{Bmatrix}
e_{X'} \times r_{T1'} & e_{Y'} \times r_{T1'} & e_Z \\
e_{X'} \times r_{T2'} & e_{Y'} \times r_{T2'} & e_Z \\
e_{X'} \times r_{T3'} & e_{Y'} \times r_{T3'} & e_Z
\end{Bmatrix} (3 - \text{leg mechanism}) \\[4ex]
\begin{Bmatrix}
e_{X'} \times r_{T1'} & e_{Y'} \times r_{T1'} & e_Z & e_{Z'} \\
e_{X'} \times r_{T2'} & e_{Y'} \times r_{T2'} & e_Z & e_{Z'} \\
e_{X'} \times r_{T3'} & e_{Y'} \times r_{T3'} & e_Z & e_{Z'} \\
e_{X'} \times r_{T4'} & e_{Y'} \times r_{T4'} & e_Z & e_{Z'}
\end{Bmatrix} (4 - \text{leg mechanism})
\end{cases}
\tag{7}
$$

where $\dot{X}$ is the speed matrix of the VMP, $\dot{q}$ is the velocity of driving joints, Jq is the driving Jacobian matrix, V_T is the velocity matrix of contact points, J_X is the output Jacobian matrix, $e_{X'}$, $e_{Y'}$, and $e_{Z'}$ are the unit vectors corresponding to the X'-, Y'-, and Z'- axes of the VMP, e_Z is the unit vector of the Z-axis corresponding to the base, and $r_{Ti'}$ is the vector from the VMP center to the ith contact point.

3.2. Comprehensive Performance analysis

According to the introduction of the functional task in Section 2.1, this paper will mainly study four performance indexes of the VEPM, including the workspace, the stiffness, the motion transmission, and the stability.

3.2.1. Workspace

The workspace is a collection of the reachable areas of the mechanism. Monte Carlo method [42] is a classical method to solve the workspace by traversing all points in the space. However, it is unsuitable for solving the workspace with a functional task. So, a task-oriented Monte Carlo method is proposed in this paper.

First, according to the fitting surface formula at the terrain point and the workspace of the original kinematic chain in the ECM, a feasible touch point set can be solved. Second, the driving variables of the ECM can be solved through the inverse kinematics. By judging whether the driving variable satisfies the stroke requirements, it is judged whether the touch point belongs to the workspace of the ECM. If the stroke requirements are satisfied, the motion variables of the VMP can be obtained based on the forward kinematics. By traversing the entire terrain map and integrating the motion variables of the VMP, the task-oriented workspace volume V_T can be obtained, as shown in Eq. (7).

$$V_T = \int_T dW \tag{8}$$

3.2.2. Stiffness analysis

The static stiffness index [11, 43] determines the motion accuracy and structural stability of a mechanism. When the stiffness index of the VEPM is larger, it means that the motion error caused by the external force is smaller, that the current configuration of the VEPM is farther away from the singular configurations, and that adaptability of the VEPM to the terrain is stronger. The stiffness matrix of the VEPM can be solved by Jacobian matrix. This paper takes the mean value of the diagonal elements in the stiffness matrix as the local stiffness index S_{tl}. The integral value of all the local stiffness index on the terrain map is used as the global stiffness index S_{tg} of the VEPM, as shown in Eq. (8).

$$K = J^T k J$$
$$S_{tl} = E(tr(K))$$
$$S_{tg} = \int_T S_{tl} dW / V_T \tag{9}$$

where K is the stiffness matrix, $J = J_q^{-1} \cdot J_X$ is the Jacobian matrix, k is the stiffness matrix of the joint space, $E()$ is the mean function, and $t_r()$ is a vector made up with the matrix diagonal elements.

3.2.3. Motion/force transmission analysis

The motion/force transmission [16, 17, 44] reflects the transfer efficiency between the input and output variables of the VEPM model. When the motion/force transmission index is higher, the ability of the ECM to adapt the terrain changes is stronger. The motion transmission index can be solved by analyzing the motion screw of the VEPM. The motion screw $\$_{Ap,i}$, $\$_{Tp,i}$ and $\$_{Op,i}$ of the physical kinematical chain in the VEPM should be solved with the actual configuration and dimensional parameters of the ECM. The input motion screw $\$_{Av,i}$ of the virtual kinematical chain in the VEPM is the output motion screw $\$_{Op,i}$ of the physical kinematical chain. The transmission wrench $\$_{Tv,i}$ of the virtual kinematical chain is a constraint force screw perpendicular to the datum plane of the VMP, as shown in Eq. (9).

$$\$_{Tv,i} = \{O; e_{z'}\} \tag{10}$$

The calculation of the output motion screw $\$_{voi,j}$ in the virtual kinematical chain is different according to the VMP's structure. For three-leg ECMs, the output motion of the VMP is a multiple motion including one rotation motion and one plane motion. The rotation is along the axis passing through the other two contact points. The plane motion is a 3-DOFs motion in the datum plane of the VMP, as shown in Eq. (10).

$$\begin{cases} \$_{voi,1} = \left\{ e_{i+1,i+3}; r_{P,i+2} \times e_{i+2,i+4} \right\} \\ \$_{voi,2} = \{O; e_{x'}\} \\ \$_{voi,3} = \{O; e_{y'}\} \\ \$_{voi,4} = \left\{ e_{z'}; r_{P,i} \times e_{z'} \right\} \end{cases} \tag{11}$$

where $e_{i,j}$ is the unit vector from ith contact point to jth contact point, and $r_{P,k}$ is the vector from original point to kth contact point.

For four-leg ECMs, the output motion of the moving platform is also a multiple motion including one rotation motion and one plane motion. The rotation axis passes through the diagonal contact point and is parallel to the vector passing through the two adjacent contact points. The plane motion is a 3-DOFs motion in the datum plane of the main-VMP, as shown in Eq. (11).

$$\begin{cases} \$_{voi,1} = \left\{ e_{i+1,i+3}; r_{P,i+2} \times e_{24} \right\} \\ \$_{voi,2} = \{O; e_{x'}\} \\ \$_{voi,3} = \{O; e_{y'}\} \\ \$_{voi,4} = \left\{ e_{z'}; r_{P,i+2} \times e_{z'} \right\} \end{cases} \tag{12}$$

Meanwhile, the motion of the VMP is also constrained by the VRC. Therefore, the output motion screw needs to be reciprocal with the constraint screw $\$r\,m,i$ of the VMP, as shown in Eq. (12).

$$\begin{cases} \$_{m,1}^r = \{e_{x'}; r_P \times e_{x'}\} \\ \$_{m,2}^r = \{e_{y'}; r_P \times e_{y'}\} \\ \$_{m,3}^r = \{O; e_z\} \end{cases} \tag{13}$$

The local motion/force transmission index S_{ml} of the VEPM is the minimum value among the input and output transmission indexes of all chains. The global motion/force transmission index S_{mg} of the VEPM is the integral value of the local motion/force transmission index on the terrain map, as shown in Eq. (13).

$$\lambda_i = \frac{\left|\$_{Af,i} \circ \$_{Tf,i}\right| \left|\$_{Ab,i} \circ \$_{Tb,i}\right|}{\left|\$_{Af,i} \circ \$_{Tf,i}\right|_{\max} \left|\$_{Ab,i} \circ \$_{Tb,i}\right|_{\max}}$$

$$\eta_i = \frac{\left|\$_{Of,i} \circ \$_{Tf,i}\right| \left|\$_{Ob,i} \circ \$_{Tb,i}\right|}{\left|\$_{Of,i} \circ \$_{Tf,i}\right|_{\max} \left|\$_{Ob,i} \circ \$_{Tb,i}\right|_{\max}} \qquad (14)$$

$$S_{ml} = \min\{\lambda_i, \eta_i\}$$

$$S_{mg} = \int_T S_{ml} \mathrm{d}W \Big/ V_T$$

where λ_i and η_i represent the input and output transmission index corresponding to the ith kinematic chain.

3.2.4. Stability analysis

The stability [33, 34, 45] evaluates the ability of the ECM to resist external forces and prevent overturning. The higher the stability index, the greater the external force required to overturn the ECM, and the higher the safety of the ECM. The main force of the ECM to resist the overturning is the gravity of the system. Therefore, this paper uses the ratio $k_{F_{wn}}$ of the minimum overturning force to the gravity to evaluate the stability in the external force direction, as shown in Eq. (14). The local stability index S_{sl} of the VEPM at the terrain point is the mean value of the stability index with all directions. The global stability index S_{sg} is the integral of the local stability index on the terrain map, as shown in Eq. (14).

$$k_{F_{wn}} = F_{wn} \Big/ G = \frac{\left|e_{F_{wn}} \times r_{wn} \cdot e_F\right|}{\left|e_Z \times r_{wn} \cdot e_F\right|}$$

$$S_{sl} = \mathrm{mean}\left(k_{F_{wn}}\right), \theta_Z \in [0, 2\pi] \qquad (15)$$

$$S_{sg} = \int_T S_{sl} \mathrm{d}W \Big/ V_T$$

where F_{wn} is the external force, G is the gravity, $e_{Fwn} = \{\cos[\theta_z], \sin[\theta_z], 0\}$ is the unit vector with the direction of the external force, θ_z is the angle between the X-axis of the base and the external force direction, and e_F is the unit vector corresponding to the flip axis.

3.3. Hybrid optimization method

The dimension synthesis of a mechanism is essentially an optimization problem [46]. The optimization takes the comprehensive performance index of the mechanism as the objective function and solves the optimal structural dimension of the mechanism. The kinematics analysis and performance calculation of the VEPM involve a large number of high-order nonlinear calculations. So, the Brute-Force method that solves the optimal solution by traversing all feasible solution is unsuitable to solve the dimension optimization of the VEPM. Therefore, many advanced optimization solutions such as the genetics [47], the particle swarm optimization [48], and the neural network algorithm [49] are introduced into the dimension optimization of the mechanism.

In this paper, the target of the dimension optimization is the specific functional task, and the task is described with the DEM model. The comprehensive performance index of the VEPM is established on the DEM model. According to the specific task, the size of the DEM map is different. For lunar
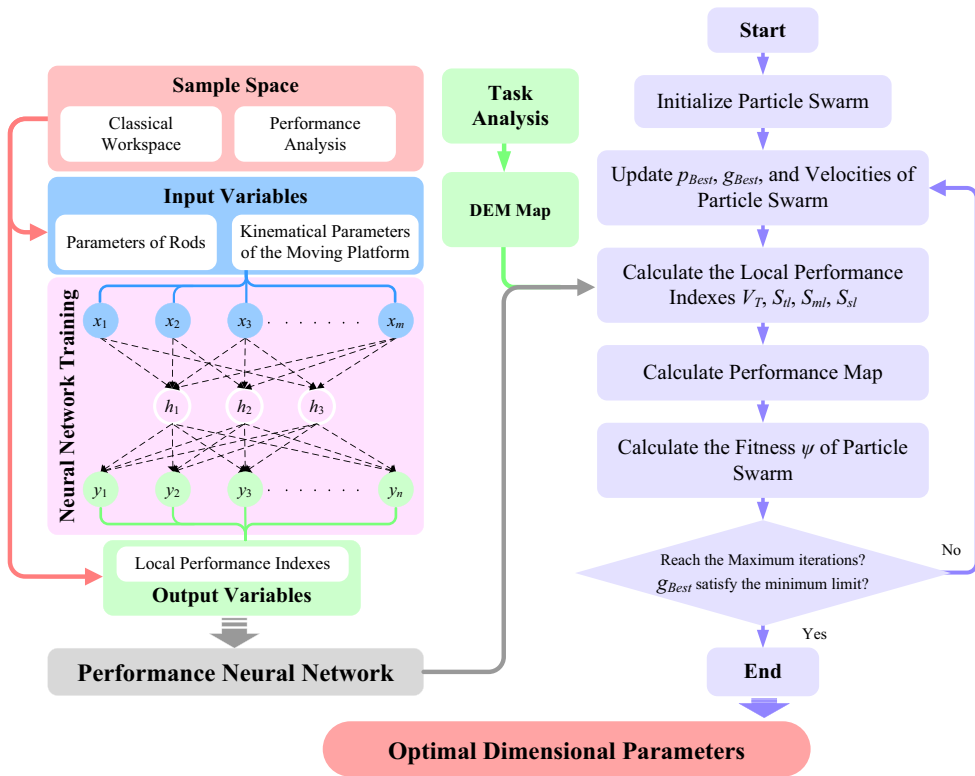
Figure 4. *The flowchart of the task-oriented comprehensive optimization algorithm.*
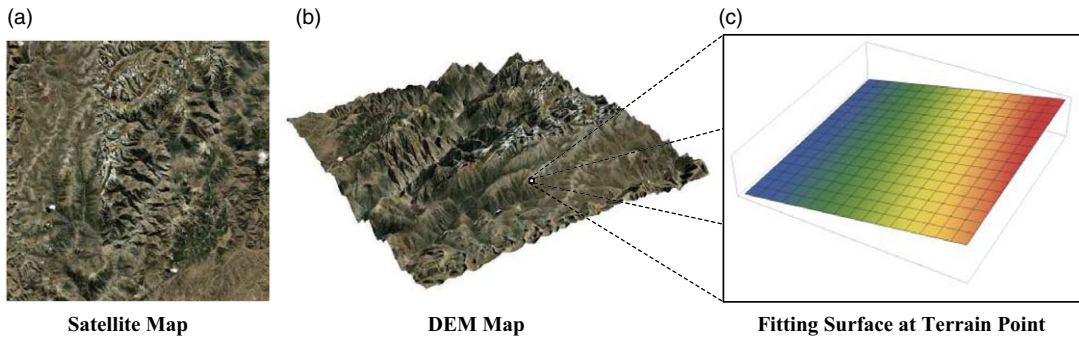
exploration project, lunar surface area is about 3.79×1013 m^2, and the number of terrain points is astronomical. Obviously, traversing the entire terrain map for the optimal solution will consume a huge number of computing resources. Thus, this paper proposes a new hybrid optimization algorithm based on the particle swarm algorithm and the neural network algorithm. The flowchart of the new optimization algorithm is shown in Fig. 4. The entire optimization algorithm can be divided into two parts: the preparation and the optimization.

In the preparation stage, the nonlinear calculation of the VEPM's performance index will be converted into the linear calculation of a neural network. The core of the preparation phase is the training of the neural network. The samples of the neural network are collected form the performance analysis with the classical workspace. The input parameters of the sample are the motion variables of the VMP and the rod dimensions of the ECM. The output parameters of the sample are the performance indexes of the VEPM. The trained neural network is used to replace the calculation of the VEPM's performance indexes.

In the optimization stage, this paper uses the particle swarm optimization algorithm to solve the optimal solution. First, a group of random particles are initialized, and their fitness value are calculated. The fitness value is the comprehensive performance index Ψ of the VEPM, as shown in Eq. (15).

$$\psi = k_1 \frac{V_W}{\max(V_W)} + k_2 \frac{S_{tg}}{\max(S_{tg})} + k_3 \frac{S_{mg}}{\max(S_{mg})} + k_4 \frac{S_{sg}}{\max(S_{sg})} \tag{16}$$

where max(t) is the maximum value of t from the first iteration to the last iteration. $k_i (0 \leq k_i \leq 1)$ is the scale factor, and its value is determined based on the task requirement of the landing gear.

(a)   (b)   (c)

Satellite Map   **DEM Map**   **Fitting Surface at Terrain Point**

Figure 5. *The satellite map (a), the DEM map (b), and the fitting terrain surface (c).*

Then, all the particles are updated through the update function (as shown in Eq. (16)), and the optimal solution of the particle and the optimal solution among the entire particles are calculated and updated. Finally, through continuous iteration and update, the global optimal solution will be the output.

$$\begin{cases} p_{i,k} = p_{i,k-1} + v_{i,k} \\ v_{i,k} = c \cdot v_{i,k-1} + \text{rand} \cdot \left(p_{g,Best} - p_{i,k}\right) + \text{rand} \cdot \left(p_{i,Best} - p_{i,k}\right) \\ c = 0.5(i_{max} - k) / i_{max} \end{cases} \tag{17}$$

where $p_{i,k}$ and $v_{i,k}$ are the value and speed of the ith particle in the kth iteration, $p_{g,Best}$ is the value of the global optimal particle, and $p_{i,Best}$ is the optimal value of the ith particle.

4. Case analysis

To further illustrate the application of the task-oriented optimization approach proposed in this paper, this section applies a specific case to introduce the application process in detail.

4.1. Case introduction

There is a wide forested area in the western part of China. Due to the high altitude and sparsely population, this area is rich in natural resources [50]. To explore the resources in this area, the robot with the vertical taking-off and landing function can improve the detection efficiency [51]. Considering that most of this area is unstructured terrain, so the robot is required to have a high terrain adaptability. This paper takes the terrain-adaptive landing gear as a case to optimize its dimensions.

This paper randomly selects the map of Zuogong City, Xinjiang Province as the functional task. The terrain map is supported for free by Bigmaper. The satellite map and the three-dimensional model of the terrain map are shown in Fig. 5.

To comprehensively compare the performance of the landing gear with the three-leg and four-leg layouts (as shown in Fig. 6), this paper optimizes the two layout mechanisms. There are two engineering requirements in the design of the landing gear mechanism. The first one is the sufficient output stroke of the mechanism. The second one is the energy conservation that requires the driving joint of the mechanism having a self-locking function. Therefore, this paper uses a combination of a parallelogram mechanism and a link-slider mechanism as the kinematical chain of the landing gear, as shown in Fig. 6.

4.2. Kinematical model and dimension optimization

According to the introduction in Section 3, the VEPM models of the three-leg ECM and the four-leg ECM can be constructed, as shown in Fig. 7.
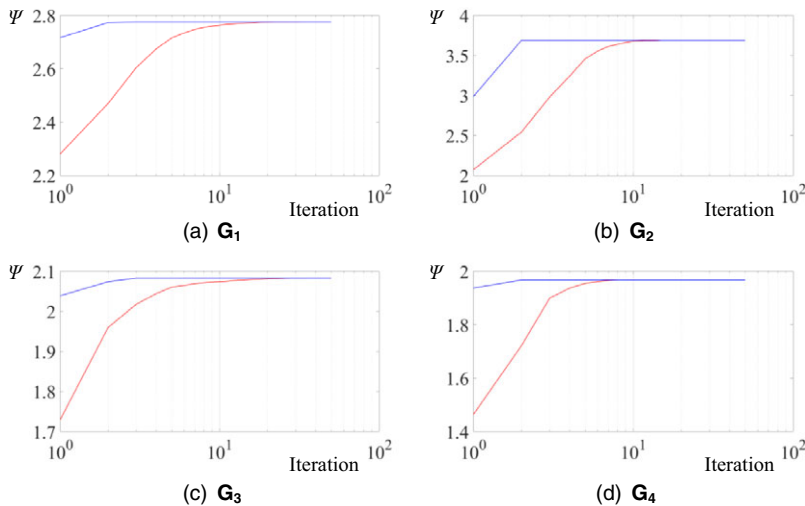
Figure 6. *Physical models of the three-leg (a) and four-leg (b) landing gear mechanisms and kinematic chain (c).*

Figure 7. *The VEPM models of the three-leg and four-leg landing gear mechanisms.*

Figure 8. *The optimization processes of* G1 *(a)*, G2 *(b)*, G3 *(c)*, G4 *(d)*.

Based on the structure of the kinematic chain, its kinematical model can be obtained through the vector method, as shown in Eq. (17). Combined with the introduction in Section 3, the kinematical model and Jacobian matrix of the two VEPM models can be obtained.

$$p_{z,i} = F_f(l) = \frac{2r_c}{r_a}\sqrt{r_a^2 - l^2 \Big/ 4} \tag{18}$$

where $p_{z,i}$ is the Z-axis coordinate of the ith touch point, l is the length of the driving slider, and r_a and r_c are rod lengths.

To reduce the impact of objective conditions on the comparative experiment, this paper sets the layout of the ECMs to be symmetrically distributed around the center of the base. The distance from the connecting point of the kinematic chain to the base center is 500 mm. The value ranges and constraint conditions of the rods in the ECMs are shown in Eq. (18).
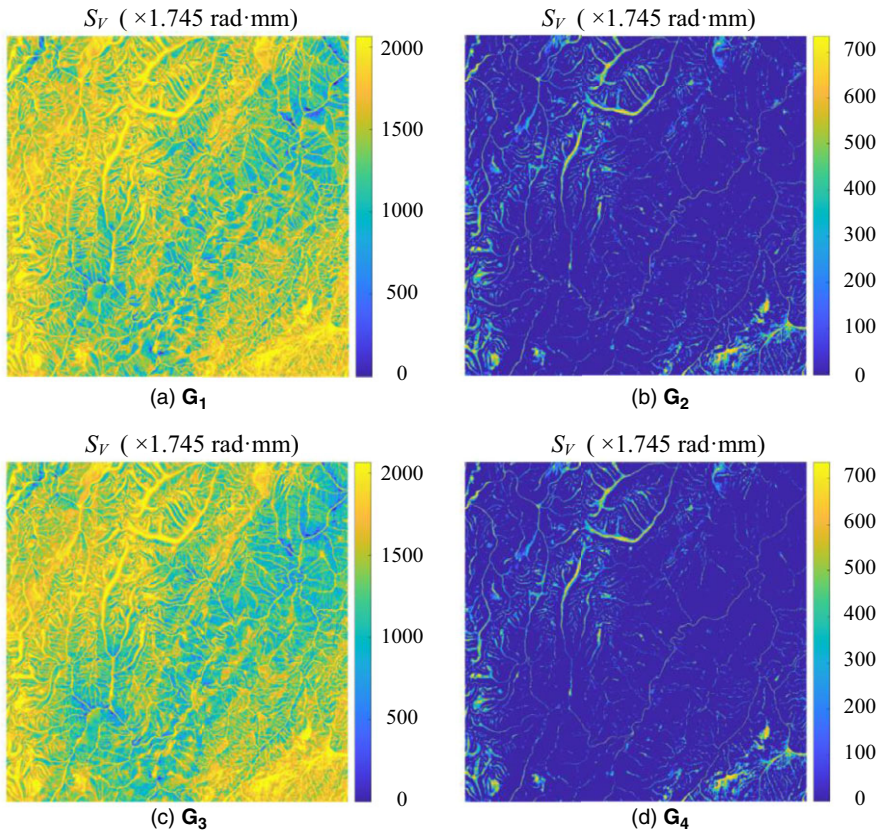
$$
\begin{aligned}
&100\,\text{mm} \le r_a \le 160\,\text{mm} \\
&100\,\text{mm} \le r_b \le 160\,\text{mm} \\
&r_a = r_d \\
&r_c = r_a + r_b
\end{aligned}
\tag{19}
$$

To compare and analyze the improvement of the new optimization approach in the ECM's performance and to analyze the difference in the performance between the three-leg and four-leg layouts, four group experiments are set up in this case. Among them, the first (G1) and second (G2) groups correspond to the three-leg layout, while the third (G3) and fourth (G4) groups correspond to the four-leg layout. The mechanisms in G1 and G3 are optimized with the task-oriented optimization method proposed in this paper, while the mechanisms in G2 and G4 are optimized based on the classical workspace.

In the optimization processes, all the scale factors in the comprehensive performance index Ψ are set to 1, and 100 iterations with 100 particles are applied to the particle swarm optimization. The optimization processes of the four group experiments are shown in Fig. 8. In the result figures, the horizontal axis represents the number of iterations, while the vertical axis represents the fitness value. The blue curves represent the global optimal fitness value, while the red curves represent the average value of the optimal fitness values in all particles. It can be seen from the results that the particle swarm has obtained the global optimal solution before the 10th iteration, and all the particles reached the global

Table I. *The dimension optimization results.*

	3-leg mechanism		4-leg mechanism	
Rods (mm)	**VEPM optimization G1**	**workspace optimization G2**	**VEPM optimization G3**	**workspace optimization G4**
r_a	157.5	160	158.6	160
r_b	160	100	160	100

S_V (×1.745 rad·mm)

(a) **G₁**

(b) **G₂**

(c) **G₃**

(d) **G₄**

Figure 9. *The workspace maps of the* G1 *(a),* G2 *(b),* G3 *(c),* G4 *(d).*

optimal solution before the 100-th iteration. The optimization results of the four group experiments are shown in Table I.

4.3. Comprehensive performance analysis

This section analyzes the performance of the VEPMs in four group experiments in detail.

Figure 9 shows the workspace map of the results. The horizontal and vertical axes, respectively, represent the latitude and longitude coordinates of the satellite map. The color value represents the area of the workspace at the coordinates. When a terrain point is given, the ECM's posture changes with the changes of the azimuth angle θ_d (the angle between the X-axis of the base frame in the ECM and the north direction) and the ground clearance h_c. The aggregate of all the feasible azimuth angle and the ground clearance is expressed by the area. The result figures show that the workspace areas of G2 and

Table II. *The summary of the experiment results.*

Performances	Summaries	
	Superiority	**G2 > G4 > G1 > G3**
Stiffness	The stiffness performance with classical workspace optimization is better than that with task-oriented optimization; The stiffness performance of the three-leg layout is better than that of the four-leg layout; The change of the azimuth angle has limited influence on the stiffness performance; The ground clearance has a greater influence on the stiffness performance of the mechanism.	
	Superiority	**G4 > G2 > G1 > G3**
Motion/force transmission	The classical workspace optimization behaves slightly better than the task-oriented optimization in the motion/force transmission; The four-leg layout performs better than the three-leg layout; The change of the azimuth angle has less influence in the motion/force transmission performance; The ground clearance has a greater influence in the motion/force transmission performance.	
	Superiority	**G3 > G2 > G1 > G4**
Stability	The stability performance of the task-oriented optimization is slightly better than that of the classical workspace optimization; The four-leg layout performs significantly better than the three-leg layout in the stability performance; The changes of the azimuth angle and the ground clearance have a greater impact on the stability performance of the mechanism.	

G4 are significantly larger than those of G1 and G3. The results show that the task-oriented optimization method can better adapt to the terrain task. Longitudinal comparison shows that the workspace areas of G1 and G2 are slightly larger than those of G3 and G4. The results show that the workspace of the three-leg layout is larger than that of the four-leg layout.

Like the analysis of the workspace, the local stiffness, the motion/force transmission index, and the local stability index are simulated, and the specific results are presented in Appendix A-C. Combined with the results, some conclusions can be summarized and listed in Table II.

To quantitatively compare the results of the four group experiments, the global performance indexes based on the terrain map are solved, and the results are shown in Table III.

The result table shows that the classical workspace optimization has obvious advantages in the stiffness and the motion/force transmission with the great expense of the ECM's workspace. On the other hand, the three-leg layout is superior to the four-leg layout in the stiffness and motion/force transmission. The results are not completely consistent with the results of the local performance analysis above, because the two layouts have different distributions in the local performance indexes.

4.4. Case summary

By analyzing the results of the four groups experiments, the following conclusions can be summarized:

(1) The task-oriented optimization can significantly increase the terrain adaptability of the ECM.
(2) The local performance indexes of the mechanism are less affected by the azimuth angle and more affected by the ground clearance.

Table III. *The global performance indexes.*

	G1	G2	G3	G4
S_W/S_T	99.98%	15.93%	99.98%	13.4%
$V_T(\text{km}^2 \cdot \text{m} \cdot \text{rad})$	5415.0	147.9	5219.4	125.9
S_{mg}	0.2034	0.4281	0.1551	0.5020
$S_{tg}(\text{kNm/rad})$	352.53	677.35	115.50	574.32
S_{sg}	1.97	2.28	3.13	1.02

(3) The three-leg layout performs better than the four-leg layout in mechanism's kinematical performance.

(4) The four-leg layout is better than the three-leg layout in the stability.

(5) The workspace of the three-leg layout is slightly better than that of the four-leg layout.

The comparison and analysis of the performance between different layouts can guide the layout design of the ECM. For example, a three-legged layout can be selected to quickly respond to the terrain changes in the areas with steep terrains. In the area with flat terrains, a four-leg layout can be used to obtain greater stability and safety performance.

5. Conclusion

Focusing on the functional task of the ECM, this paper proposes a task-oriented comprehensive performance optimization approach based on the virtual equivalent parallel mechanism. The new approach uses the comprehensive performance index of the ECM at the target terrain area as the digital quantification of the functional task. Based on the virtual equivalent parallel mechanism, the mapping relationship between the DEM map and the comprehensive performance index of the VEPM is established. Taking the global performance index as the optimization target, a task-oriented comprehensive performance optimization algorithm is proposed based on the particle swarm algorithm and the neural network algorithm. The superiorities of the new approach are verified with a comparative experiment.

The new approach can be applied to the dimensional synthesis of the ECM and its control system design. The new approach can directly calculate the comprehensive performance indexes of the ECM based on the terrain data. The calculation results can be used to improve the comprehensive performance of the ECM. The performance indexes can also be used in the design of the optimal control system. The visualized local performance map can help the ECM's operator to make the optimal decision. On the other hand, there will be a larger number of nonlinear calculations when the VEPM model is applied into the optimization, which will reduce the real-time performance of the system. We will fix the real-time problem in our future study.

Author contributions. Conceptualization, D.Z., H.T., J.Z.; methodology, D.Z., H.T.; software, H.T., J.Z.; formal analysis, D.Z., H.T., J.Z.; investigation, J.Z., H.T.; writing-original draft preparation, H.T.; writing-review & editing, D.Z., J.Z.

Declaration of competing interest. The authors declare that they have no known competing financial interests of personal relationships that could have appeared to influence the work reported in this paper.

References

[1] K. V. Reddy, M. Kodati, K. Chatra and S. Bandyopadhyay, "A comprehensive kinematic analysis of the double wishbone and MacPherson strut suspension systems," *Mech. Mach. Theory* **105**(7), 441–470 (2016).

[2] H. Luo and J. Zhao, "Synthesis and kinematics of a double-lock overconstrained landing gear mechanism," *Mech. Mach. Theory* **121**(1), 245–258 (2018).

[3] Y. Han, W. Guo, F. Gao and J. Yang, "A new dimension design method for the cantilever-type legged lander based on truss-mechanism transformation," *Mech. Mach. Theory* **142**(1–4), 103611 (2019).

[4] J. Han, D. Kitazawa, T. Kinoshita, T. Maeda and H. Itakura, "Experimental investigation on a cabin-suspended catamaran in terms of motion reduction and wave energy harvesting by means of a semi-active motion control system," *Appl. Ocean Res.* **83**(3–5), 88–102 (2019).

[5] L. Li, Y. Fang, S. Guo and L. Wang, "Type synthesis of a class of novel 3-DOF single-loop parallel leg mechanisms for walking robots," *Mech. Mach. Theory* **145**(5), 103695 (2020).

[6] P. Biswal and P. K. Mohanty, "Modeling and effective foot force distribution for the legs of a quadruped robot," *Robotica* **39**(8), 1504–1517 (2021).

[7] M. Russoa, S. Herrero, O. Altuzarra and M. Ceccarelli, "Kinematic analysis and multi-objective optimization of a 3-UPR parallel mechanism for a robotic leg," *Mech. Mach. Theory* **120**(1850), 192–202 2018 (2018).

[8] M. Ceccarelli. *Fundamentals of Mechanics of Robotic Manipulation* (Springer, Dordrecht, 2004).

[9] R. Kelaiaia, O. Company and A. Zaatri, "Multiobjective optimization of a linear delta parallel robot," *Mech. Mach. Theory* **50**(1), 159–178 (2012).

[10] B. Jiang, H. Fang and H. Zhang, "Type synthesis and kinematics performance analysis of a class of 3T2R parallel mechanisms with large output rotational angles," *Int. J. Automat. Comput.* **16**(6), 775–785 (2019).

[11] D. Zhang and Z. Gao, "Forward kinematics, performance analysis, and multi-objective optimization of a bio-inspired parallel manipulator," *Robot. Comput.-Integr. Manuf.* **28**(4), 484–492 (2012).

[12] Y. Zhang, X. Wang, Y. Xin, Y. Wu, M. Kang and X. Wang, "Quadruped robot leg optimization based on a multi-objective genetic algorithm," *Mechanika* **23**(6), 881–890 (2017).

[13] Y. Han, W. Guo, Z. Peng, M. He, F. Gao and J. Yang, "Dimensional synthesis of the reconfigurable legged mobile lander with multi-mode and complex mechanism topology," *Mech. Mach. Theory* **155**, 104097 (2021).

[14] C. Gosselin, "Determination of the Workspace of 6-DOF Parallel Manipulators," **In:** *International Design Engineering Technical Conferences and Computers and Information in Engineering Conference* (1989) pp. 321–326.

[15] J. Wang, C. Wu and X. Liu, "Performance evaluation of parallel manipulators: Motion/force transmissibility and its index," *Mech. Mach. Theory* **45**(10), 1462–1476 (2010).

[16] J. Brinker, B. Corves and Y. Takeda, "Kinematic performance evaluation of high-speed delta parallel robots based on motion/force transmission indices," *Mech. Mach. Theory* **125**(1), 111–125 (2018).

[17] X. Liu, J. Wang and G. Pritschow, "Performance atlases and optimum design of planar 5R symmetrical parallel mechanisms," *Mech. Mach. Theory* **41**(2), 119–144 (2006).

[18] Z. Chong, F. Xie, X. Liu and J. Wang, "Evaluation of dynamic isotropy and coupling acceleration capacity for a parallel manipulator with mixed DoFs," *Mech. Mach. Theory* **163**(6), 104382 (2021).

[19] D. Zhang and B. Wei, "Global Stiffness and Well-Conditioned Workspace Optimization Analysis of 3UPU-UPU Robot Based on Pareto Front Theory," **In:** *International Conference on Cooperative Design, Visualization and Engineering* (2015) pp. 124–133.

[20] R. Lin, W. Guo, X. Chen and M. Li, "Type synthesis of legged mobile landers with one passive limb using the singularity property," *Robotica* **36**(12), 1836–1856 (2018).

[21] T. Niessing and X. Fang, "Kinematic analysis and optimisation of a novel multi-link torsion axle," *Mech. Mach. Theory* **165**(5), 104432 (2021).

[22] M. Issa and A. Samn, "Passive vehicle suspension system optimization using Harris Hawk optimization algorithm," *Math. Comput. Simulat.* **191**(2), 328–345 (2022).

[23] M. Edgar, L. Erik and T. Rafael, "A multi-configuration kinematic model for active drive/steer four-wheel robot structures," *Robotica* **34**(10), 2309–2329 (2016).

[24] G. Yu, J. Wu, L. Wang and Y. Gao, "Optimal design of the three-degree-of-freedom parallel manipulator in a spray-painting equipment," *Robotica* **38**(6), 1064–1081 (2020).

[25] J. Wu, X. Wang, B. Zhang and H. Tian, "Multi-objective optimal design of a novel 6-DOF spray-painting robot," *Robotica* **39**(12), 2268–2282 (2021).

[26] X. Wan and H. Zhang, "Optimization design of a walkable fixture mechanism," *J. Manufact. Sci. Eng.* **140**(8), 081002 (2018).

[27] G. Wu, S. Bai and P. Hjørnet, "Architecture optimization of a parallel Schönflies-motion robot for pick-and-place applications in a predefined workspace," *Mech. Mach. Theory* **106**(2), 148–165 (2016).

[28] J. Kim, F. C. Park, S. J. Ryu, J. Kim, J. Hwang, C. Park and C. Iurascu, "Design and analysis of a redundantly actuated parallel mechanism for rapid machining," *IEEE Trans. Robot. Autom.* **17**(4), 423–434 (2001).

[29] R. Cao, F. Gao, Y. Zhang, D. Pan and W. Chen, "A new parameter design method of a 6-DOF parallel motion simulator for a given workspace," *Mech. Des. Struct. Mach.* **43**(1), 1–18 (2015).

[30] A. Stelzer, H. Hirschmüller and M. Görner, "Stereo-vision-based navigation of a six-legged walking robot in unknown rough terrain," *Int. J. Robot. Res.* **31**, 381–402 (2012).

[31] M. Wermelinger, P. Fankhauser, R. Diethelm, P. Krüsi, R. Siegwart and M. Hutter, "Navigation Planning for Legged Robots in Challenging Terrain," **In:** *IEEE/RSJ International Conference on Intelligent Robots and Systems* (2016) pp. 1184-1189.

[32] H. Tang, D. Zhang and Z. Gan, "Control system for vertical take-off and landing vehicle's adaptive landing based on multi-sensor data fusion," *Sensors* **20**, 4411 (2020).

[33] H. Tang, D. Zhang and C. Tian, "An approach for modeling and performance analysis of Three-Leg landing gear mechanisms based on the virtual equivalent parallel mechanism," *Mech. Mach. Theory* **169**, 104617 (2021).

[34] H. Tang, D. Zhang and C. Tian, "A method for comprehensive performance optimization of Four-Leg landing gear based on the virtual equivalent parallel mechanism," *Mech. Mach. Theory* **174**, 104924 (2022).

[35] J. Liu, D. Zhang, C. Wu, H. Tang and C. Tian, "A multi-finger robot system for adaptive landing gear and aerial manipulation," *Robot. Autonom. Syst.* **146**(3), 103878 (2021).

[36] J. Liu, D. Zhang, Y. Chen, Z. Xia and C. Wu, "Design of a class of generalized parallel mechanisms for adaptive landing and aerial manipulation," *Mech. Mach. Theory* **170**(2), 104692 (2022).

[37] N. Likar, B. Nemec and L. Žlajpah, "Virtual mechanism approach for dual-arm manipulation," *Robotica* **32**(6), 713 (2014).

[38] E. Ozgur, G. Gogu and Y. Mezouar, "Structural Synthesis of Dexterous Hands," **In:** *IEEE/RSJ International Conference on Intelligent Robots and Systems* (2014) pp. 1676-1681.

[39] Y. Hu and W. Guo, "A new concept of contact joint to model the geometric foot-environment contacts for efficiently determining possible stances for legged robots," *Mech. Mach. Theory* **162**(2), 104327 (2021).

[40] S. Arnold, M. Pfrender and A. Jones, "The adaptive landscape as a conceptual bridge between micro-and macroevolution," *Genetica* **112**(1), 9–32 (2001).

[41] D. Wolock and C. Price, "Effects of digital elevation model map scale and data resolution on a topography-based watershed model," *Water Resour. Res.* **30**(11), 3041–3052 (1994).

[42] J. Rastegar and B. Fardanesh, "Manipulation workspace analysis using the Monte Carlo method," *Mech. Mach. Theory* **25**(2), 233–239 (1990).

[43] P. Lin, W. Shieh and D. Chen, "A stiffness matrix approach for the design of statically balanced planar articulated manipulators," *Mech. Mach. Theory* **45**(12), 1877–1891 (2010).

[44] X. Shen, L. Xu and Q. Li, "Motion/Force constraint indices of redundantly actuated parallel manipulators with over constraints," *Mech. Mach. Theory* **165**(4), 104427 (2021).

[45] E. P. Poulakakis and M. Buehler, "On the Stable Passive Dynamics of Quadrupedal Running," **In:** *IEEE International Conference on Robotics and Automation* (2003) pp. 1368–1373.

[46] A. Vasiliu and B. Yannou, "Dimensional synthesis of planar mechanisms using neural networks: application to path generator linkages," *Mech. Mach. Theory* **36**(2), 299–310 (2001).

[47] Y. Hou and Y. Zhao, "Workspace analysis and optimization of 3-PUU parallel mechanism in medicine base on genetic algorithm," *Open Biomed. Eng. J.* **9**(1), 214–218 (2015).
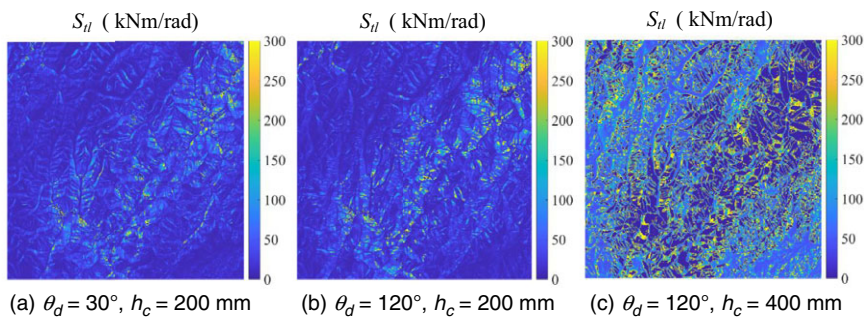
[48] R. Wang and X. Zhang, "Parameters optimization and experiment of a planar parallel 3-DOF nanopositioning system," *IEEE Trans. Ind. Electron.* **65**(3), 2388–2397 (2017).

[49] D. Zhang, "Improving the Accuracy in Software Effort Estimation: Using Artificial Neural Network Model Based on Particle Swarm Optimization," **In:** *Proceedings of 2013 IEEE International Conference on Service Operations and Logistics, and Informatics* (2013) pp. 180–185.
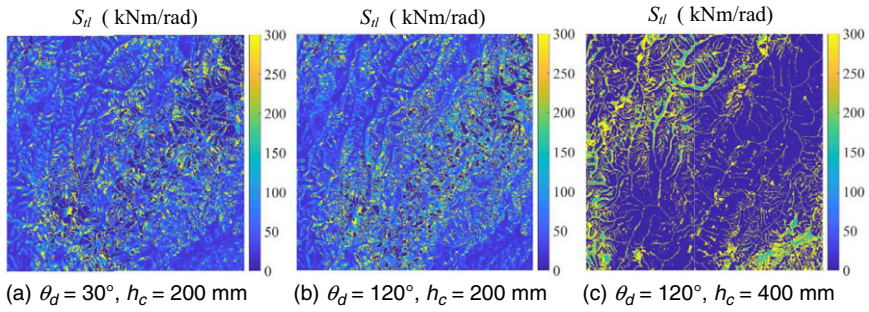
[50] Y. Yang, C. Yao and D. Xu, "Ecological compensation standards of national scenic spots in western China: A case study of Taibai Mountain," *Tour. Manag.* **76**, 103950 (2020).

[51] R. Meshcheryakov, A. Salomatin, D. Senchuk and A. Shirokov. *Scenario of Search, Detection, and Control of Invasive Plant Species Using Unmanned Aircraft Systems, Agriculture Digitalization and Organic Production* (Springer, Singapore, 2022) pp. 259–270.
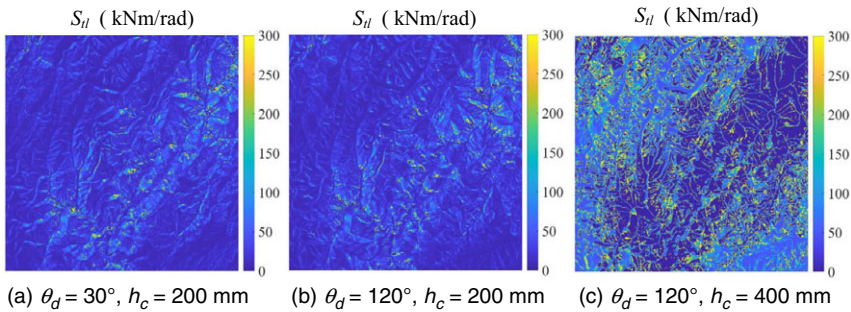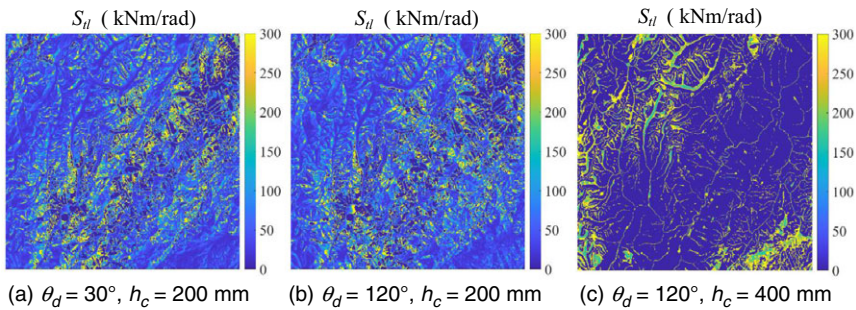
Appendix A. Local stiffness results

(a) $\theta_d = 30°$, $h_c = 200$ mm   (b) $\theta_d = 120°$, $h_c = 200$ mm   (c) $\theta_d = 120°$, $h_c = 400$ mm

Figure A1. *The local stiffness index map of* G1 *with different landing postures.*

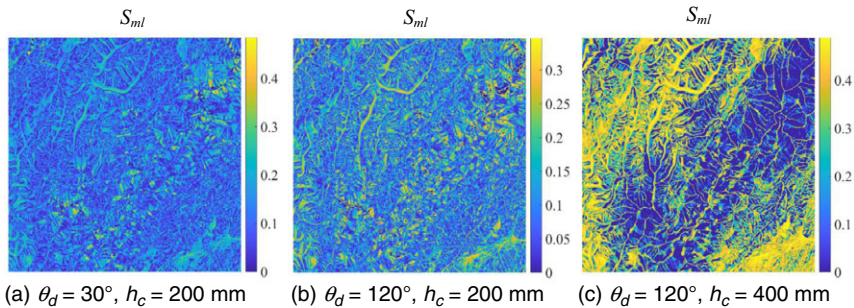**Figure A2.** *The local stiffness index map of G2 with different landing postures.*

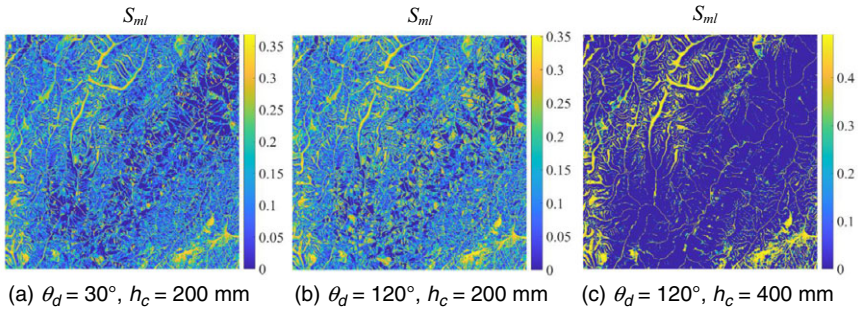**Figure A3.** *The local stiffness index map of G3 with different landing postures.*

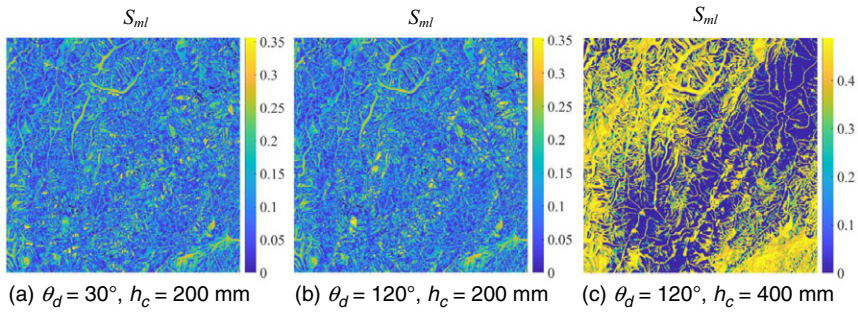**Figure A4.** *The local stiffness index map of G4 with different landing posture.*

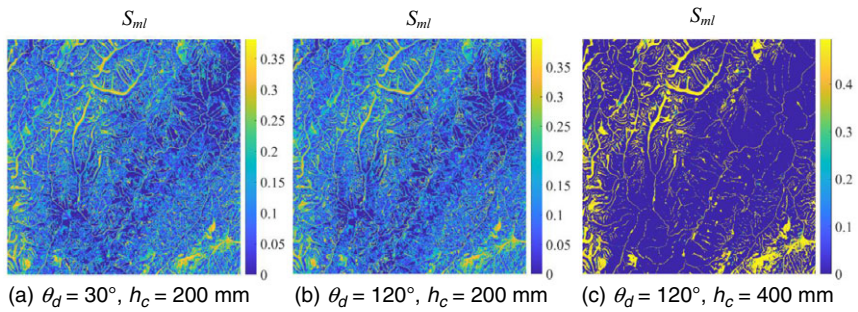## Appendix B. Local motion/force transmission results

Figure B1. *The local motion/force transmission index map of G1 with different landing postures.*

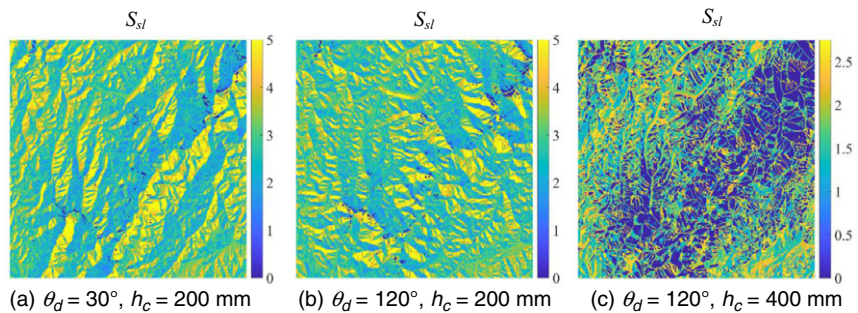**Figure B2.** *The local motion/force transmission index map of G2 with different landing postures.*

Figure B3. *The local motion/force transmission index map of G3 with different landing postures.*
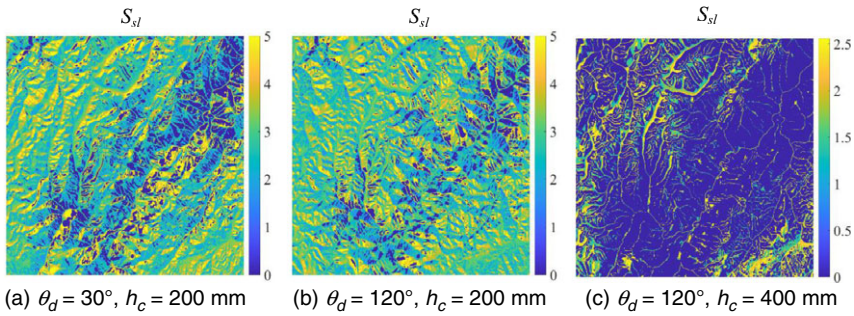

Figure B4. *The local motion/force transmission index map of G4 with different landing postures.*
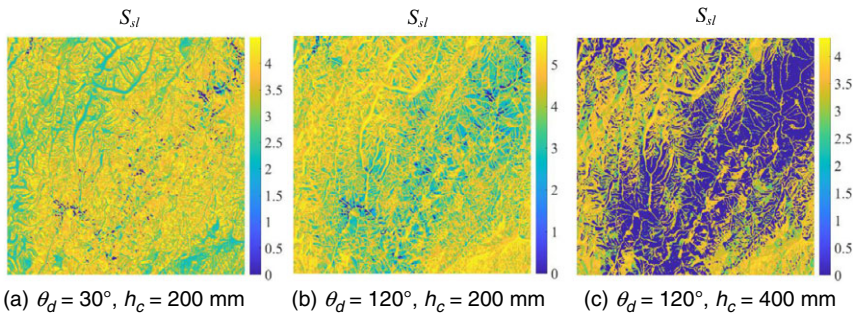
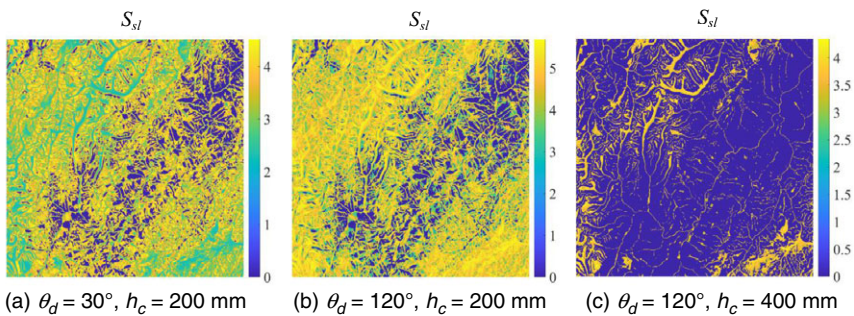## Appendix C. Local stability results

Figure C1. *The local stability index map of G1 with different landing postures.*

(a) $\theta_d = 30°$, $h_c = 200$ mm (b) $\theta_d = 120°$, $h_c = 200$ mm (c) $\theta_d = 120°$, $h_c = 400$ mm

Figure C2. *The local stability index map of G2 with different landing postures.*

(a) $\theta_d = 30°$, $h_c = 200$ mm (b) $\theta_d = 120°$, $h_c = 200$ mm (c) $\theta_d = 120°$, $h_c = 400$ mm

Figure C3. *The local stability index map of G3 with different landing postures.*

(a) $\theta_d = 30°$, $h_c = 200$ mm (b) $\theta_d = 120°$, $h_c = 200$ mm (c) $\theta_d = 120°$, $h_c = 400$ mm

Figure C4. *The local stability index map of G4 with different landing postures.*